East European Journal of Physics. **1**. 112–126 (2026)

DOI: 10.26565/2312-4334-2026-1-09 ISSN 2312-4334

BENJAMIN–FEIR INSTABILITY OF INTERFACIAL GRAVITY–CAPILLARY WAVES IN A TWO-LAYER FLUID. PART II. SURFACE-TENSION EFFECTS

Olga Avramenko[1*,2], **Volodymyr Naradovyi**[3]
[1]*National University of Kyiv-Mohyla Academy, 2 Skovorody, Kyiv, 04070, Ukraine*
[2]*Vytautas Magnus University, 58 K. Donelaičio g., Kaunas 44248, Lithuania*
[3]*Volodymyr Vynnychenko Central Ukraine State University, 1 Shevchenka, Kropyvnytskyi, 25006, Ukraine*
[*]*Corresponding Author e-mail: o.avramenko@ukma.edu.ua*

Received November 17, 2025; revised January 12, 2026; accepted February 2, 2026

This second part of the study develops a complete geometric and asymptotic description of how surface tension governs the modulational stability of interfacial waves in a two-layer fluid. Extending the analytical framework of Part I, surface tension is treated as a freely adjustable parameter, making it possible to trace the nonlinear and dispersive properties of the system across the full range of depth ratios and density contrasts. Using the nonlinear Schrödinger reduction together with long-wave asymptotics, the mechanisms that shape the boundaries between stable and unstable regimes are identified and their dependence on surface tension is quantified. The long-wave structure is controlled by two special density values that mark the bases of the loop and the corridor on the stability diagrams. Their ordering switches at a threshold that exists only when the lower layer is deeper, and loop-type structures occur only in this regime. A second organising parameter is the classical Bond threshold, at which the dispersive and nonlinear singularities coincide. When surface tension exceeds this value and the upper layer is sufficiently deep, the interaction between resonant and dispersive effects produces a capillary cut that replaces the corridor and characterises strongly capillary, upper-layer-dominated configurations. To unify these observations, the full three-dimensional critical surfaces that separate different types of nonlinear and dispersive behaviour are computed. The familiar loop, corridor, and cut appear as planar sections of these surfaces, and their transitions follow directly from the deformation of the intersection between the resonant and dispersive sheets. Two depth ratios correspond to genuine geometric degeneracies: equal layer depths, where the intersection reduces to a straight line, and the golden-ratio configuration, where the critical surface becomes horizontally tangent at the Bond threshold. Overall, Part II completes the geometric and physical classification of modulational stability in two-layer interfacial waves and provides a framework for future extensions incorporating shear, external forcing, flexible boundaries, or variable bathymetry.

Keywords: *Modulational instability; Interfacial gravity–capillary waves; Two-layer fluid; Surface tension; Benjamin–Feir instability*

PACS: 47.20.Dr, 47.20.Ky, 47.35.Bb, 47.35.Pq

1. INTRODUCTION

In Part I [1], the modulational instability of interfacial waves in a two-layer fluid was examined for different depth ratios and density contrasts under the assumption of a fixed or characteristic interfacial tension. The present paper extends that analysis by investigating the effects of varying surface tension T on the stability and topology of modulational–stability domains.

The theoretical foundation of modulational instability originates from the classical works of Benjamin and Feir [2] and Zakharov [3], with extensions to interfacial waves by Grimshaw and Pullin [4] and by Christodoulides and Dias [5]. Dullin, Gottwald, and Holm further developed a unified long-wave shallow-water asymptotic framework linking several equivalent model equations (KdV, fifth-order KdV/Kawahara, and Camassa–Holm), clarifying the role of surface tension through the Bond-number parameter and identifying the parameter regimes where each model applies [6, 7]. Building on this foundation, more recent studies have explored the influence of surface tension in both surface and interfacial systems.

Sun and Wahlén [8] performed a rigorous spectral analysis of periodic gravity–capillary waves and showed that positive T excludes spectral instabilities at high-frequency crossings, yielding regions of spectral stability.In their analysis based on the Evans function method, Hur and Yang [9] examined the spectral properties of gravity–capillary waves, identifying regimes of Wilton-ripple instability and establishing the precise criteria for their onset. Ward et al. [10] examined the Faraday instability in a system with two interfaces, demonstrating experimentally and theoretically that surface tension governs excitation thresholds.

For interfacial waves in two-layer fluids, several recent studies have derived nonlinear Schrödinger (NLS) reductions and constructed stability diagrams. Li et al. [11] obtained the NLS equation for arbitrary depths and showed that stronger density contrast and thinner layers compress the modulational–instability region, while finite T shifts the instability boundary toward shorter waves. Li et al. [12] considered a linear shear profile and demonstrated that the combined effects of shear and T alter the sign of the nonlinear coefficient, changing the envelope–stability type. Murashige and Choi [13] performed a two-dimensional stability analysis of finite-amplitude waves and found competition between modulational and Kelvin–Helmholtz instabilities: surface tension suppresses the latter but alters the width of the modulational–instability

---

Cite as: O. Avramenko, V. Naradovyi, East Eur. J. Phys. 1, 112 (2026), https://doi.org/10.26565/2312-4334-2026-1-09

band. Pal and Dhar [14, 15] produced stability maps for oceanographic parameters and emphasized the sensitivity of instability boundaries to T. Boral, Ni, and Korobkin [16] studied the interaction between interfacial and flexural–gravity waves in the presence of a discontinuous background current, while Halder et al. [17] analyzed the effect of constant vorticity and showed that vorticity and surface tension jointly modify nonlinear corrections and stability.

Other studies have explored situations where capillarity interacts with external influences. Goldobin et al. [18] investigated interfacial waves in a two-layer system subjected to horizontal vibrations and showed that surface tension T influences the onset and stability of long-wave oscillatory modes. Doak et al. [19] considered gravity–capillary waves at the boundary between dielectric fluids under an external electric field, where surface tension modifies both the dispersion relation and the stability condition. Chow, Chan, and Grimshaw [20] analyzed long internal waves in smoothly stratified shallow fluids—although surface tension was absent, their approach is directly transferable to interfacial configurations. Liang, Zareei, and Alam [21] demonstrated resonant harmonic generation in internal waves, producing narrow instability windows analogous to those induced by capillarity. Boral, Sahoo, and Stepanyants [22] investigated surface waves under wind forcing and identified T as a key control parameter for the transition between stability and instability. Andreeva, Bulavin, and Tkachenko [23] investigated the Rayleigh–Plateau dissipative instability with viscous effects in both contacting fluids and showed that surface tension, together with dissipation, controls the transition between stable and unstable regimes.

Overall, existing research provides rigorous spectral criteria for gravity–capillary waves at $T > 0$, modulational–instability maps for two-layer systems with shear and currents, and analyses of auxiliary factors such as vorticity, vibrations, electric fields, wind forcing, and stratification. However, a consistent topological classification of stability diagrams in the (ρ, k) plane under varying T has not been established. The mechanisms governing the emergence and disappearance of corridors, loops, and cuts, as well as the limiting configurations HS–La, La–HS, and HS–HS (as defined in Part I), remain insufficiently understood. These questions are addressed in the present work.

2. PROBLEM FORMULATION, PRELIMINARY BACKGROUND, AND LIMITING CASES

2.1. Mathematical formulation and background assumptions

All variables and scaling follow the notation of Part I [1].

We consider the same two-layer inviscid, incompressible fluid system as in Part I, composed of a lower layer $\Omega_1 = \{(x,z) \mid -h_1 < z < 0\}$ and an upper layer $\Omega_2 = \{(x,z) \mid 0 < z < h_2\}$, separated by the interface $z = \eta(x,t)$ with surface tension T. The fluid densities are ρ_1 and ρ_2, and the density ratio is $\rho = \rho_2/\rho_1$. In Part I, the analysis was carried out for a fixed interfacial tension corresponding to $T = 1$. Here, T is treated as a free control parameter governing the capillary contribution.

Following the nondimensionalization adopted previously, all quantities are scaled with $L = (T_0/(\rho_1 g))^{1/2}$, $t_0 = (L/g)^{1/2}$, and $m_0 = \rho_1 L^3$, where T_0 is the reference interfacial tension. The dimensionless coefficient $T = T/T_0$ measures the relative magnitude of surface tension effects. Here we keep the same nondimensionalization as in Part I, where the choice $T = T_0$ led to the dimensionless value $T = 1$ in the dispersion relation.

The governing equations for the velocity potentials $\varphi_j(x,z,t)$ and the interface displacement $\eta(x,t)$ are identical to system (1) of Part I. The dependent variables are expanded in powers of the small steepness parameter $\alpha = a/l$, where a is the maximum interface displacement and l the wavelength:

$$(\eta, \varphi_j) = \sum_{n=1}^{3} \alpha^{n-1} (\eta_n, \varphi_{jn}) + O(\alpha^3), \qquad x_n = \alpha^n x, \quad t_n = \alpha^n t.$$

From the first-order approximation, one obtains the dispersion relation

$$\omega^2 = \frac{k\,(1 - \rho + T k^2)}{\coth kh_1 + \rho\, \coth kh_2}, \tag{1}$$

in which T explicitly controls the curvature of $\omega(k)$.

At third order, the solvability condition gives the nonlinear Schrödinger equation

$$iA_t + i\omega' A_x + \tfrac{1}{2}\,\omega'' A_{xx} = -\alpha\,\omega^{-1} J\,|A|^2 A, \tag{2}$$

where $\omega' = \partial\omega/\partial k$ and $\omega'' = \partial^2\omega/\partial k^2$ are the first and second derivatives of the carrier frequency. The coefficient J is the Benjamin–Feir index, which depends on the system geometry and on the second-harmonic correction Λ (defined in Eq. (3) of Part I):

$$\begin{aligned} J = -\frac{1}{16(1-\rho)\,[\,\rho\,\coth kh_2 + \coth kh_1\,]} \Big\{ & 2k\omega^2(1-\rho)\Lambda[-3\rho\,\coth^2 kh_2 + 3\,\coth^2 kh_1 - 1 + \rho] \\ & - 4k\omega^4[\rho(\coth^2 kh_2 - 1) - (\coth^2 kh_1 - 1)]^2 \\ & - 4k^2\omega^2(1-\rho)[\rho\,\coth^3 kh_2 + \coth^3 kh_1 - 2\rho\,\coth kh_2 - 2\,\coth kh_1] - 3Tk^5(1-\rho) \Big\}. \end{aligned} \tag{3}$$

A purely temporal solution of Eq. (2), $A(t) = a\,\exp\big(i\alpha a^2\omega^{-1}Jt\big)$, with constant envelope amplitude a, is modulationally stable when

$$J\omega'' < 0, \tag{4}$$

while $J\omega'' > 0$ signals the onset of instability. In what follows, we examine how variations of T alter the loci $J = 0$ and $\omega'' = 0$ in the (ρ, k) plane, revealing new transitions between stable and unstable regimes as surface tension modifies both the nonlinear and dispersive characteristics of the interfacial mode.

2.2. Limiting case $\rho = 1$ for equal layer depths

We now consider the symmetric configuration of two layers with equal thickness $h_1 = h_2 = h$ and equal densities $\rho = 1$. In this limit the interface vanishes, and the system formally reduces to a single homogeneous fluid bounded by two free surfaces of equal curvature. Nevertheless, this configuration provides a convenient reference for analysing the nonlinear coefficient J and the structure of the Benjamin–Feir index near the symmetry line.

For $\rho = 1$ and $h_1 = h_2 = h$, substituting the dispersion relation (1),

$$\omega^2 = \frac{Tk^3}{2\,\coth kh},$$

into the general expression (3) for J, one obtains, after simplification,

$$J = -\frac{1}{32}\,T\,k^5\Big(\coth kh - \frac{5}{\cosh kh\,\sinh kh}\Big).$$

The factor T appears only as a multiplier and therefore does not affect the location of the zero of J. The condition $J = 0$ yields $\cosh^2(kh) = 5$, and hence the characteristic wavenumber at which J changes sign is

$$k_{\mathrm{ch}}(h) = \frac{1}{2h}\ln(9 + 4\sqrt{5}) \approx \frac{1.4436}{h}. \tag{5}$$

The independence of k_{ch} from the surface-tension coefficient T is a notable feature of this symmetric configuration. While T scales the dispersion relation, $\omega \propto \sqrt{T}$, so that the frequency increases as the square root of the surface tension, it does not modify the nonlinear geometry encoded in J. Consequently, the transition between focusing and defocusing nonlinearity in the Benjamin–Feir sense depends solely on the dimensionless depth parameter kh. For $k < k_{\mathrm{ch}}(h)$ the index $J > 0$, corresponding to one type of nonlinearity, whereas for $k > k_{\mathrm{ch}}(h)$ the sign reverses ($J < 0$). Because $\omega''(k)$ obeys the same scaling invariance ($\omega(k) \propto \sqrt{T}$, and thus $\omega''(k)$ scales identically and retains its sign), the overall modulational-stability criterion based on the product $J\,\omega''$ preserves the same threshold (5) for all $T > 0$.

The analytical symmetry of the perfectly symmetric configuration $\rho = 1$, $h_1 = h_2 = h$ implies that both $\omega(k)$ and $J(k)$ are even functions of the carrier wavenumber k. In this limit, the small-k expansion of the dispersion relation yields $\omega(k) \propto k^2$, so that $\omega''(k)$ tends to a finite positive constant as $k \longrightarrow 0$. By contrast, for unequal densities $\rho \neq 1$ (with comparable layer depths) the long-wave behaviour is gravity-dominated: $\omega(k) \sim c(\rho)\,k$, and hence $\omega''(k)$ vanishes linearly with k as $k \longrightarrow 0$. In both cases, the coefficient J remains finite at $k = 0$. In the long-wave regime $k \longrightarrow 0$, the critical curves associated with the conditions $J \longrightarrow \infty$ and $\omega'' = 0$ in the (ρ, k)-plane accumulate near the symmetry point $(\rho, k) = (1, 0)$. In the perfectly symmetric case $\rho = 1$, $h_1 = h_2$, both J and ω'' stay regular at $k = 0$, and the corresponding geometric degeneracy reduces to a simple linear intersection in the (ρ, k) plane, as observed in the three-dimensional representations discussed in Sec. 4.

To the best of our knowledge, the T-independence of the characteristic wavenumber k_{ch} in the symmetric limit $\rho = 1$, $h_1 = h_2$ has not been explicitly noted in the literature. This follows directly from the capillary scaling of the dispersion relation ($\omega \propto \sqrt{T}$) and the corresponding invariance of $\omega''(k)$. For a comprehensive discussion of modulational instability in gravity–capillary systems, see Dias and Kharif [25].

2.3. Mutual placement of the points ρ_{L} and ρ_{C} at $k = 0$

In the long-wave limit $k \longrightarrow 0$, the intersection points of the conditions $J = 0$ and $J \longrightarrow \infty$ with the density axis $O\rho$ are

$$\rho_{\mathrm{L}} = \frac{h_2^2}{h_1^2}, \tag{6}$$

$$\rho_{\mathrm{C}}(T) = \frac{-h_2h_1^2 + h_1h_2^2 - 3Th_1 + \sqrt{h_1^4h_2^2 + 2h_1^3h_2^3 + h_1^2h_2^4 + 6Th_1^3h_2 - 6Th_1^2h_2^2 - 12Th_1h_2^3 + 9T^2h_1^2}}{2h_1h_2^2}. \tag{7}$$

Geometry fixes the reference point $\rho_{\mathrm{L}} = h_2^2/h_1^2$, while Capillarity shifts $\rho_{\mathrm{C}}(T)$ leftward from $\rho = 1$ for small T, and, whenever the corresponding branch remains real, towards its asymptotic geometric limit for large T. The two curves intersect at a finite surface-tension value $T_\times$ defined by $\rho_{\mathrm{C}}(T_\times) = \rho_{\mathrm{L}}$. Solving this relation gives

$$T_\times = \frac{h_1^4 - h_1^3 h_2 + h_1 h_2^3 - h_2^4}{3h_1^2} = \frac{(h_1^2 - h_2^2)(h_1^2 + h_2^2 - h_1 h_2)}{3h_1^2},$$

whose sign determines the admissible configurations:

$$\operatorname{sign}(T_\times) = \begin{cases} > 0, & h_1 > h_2, \\ = 0, & h_1 = h_2, \\ < 0, & h_1 < h_2, \end{cases} \qquad \text{so that } T_\times > 0 \text{ exists only if } h_1 > h_2.$$

For physically relevant $T > 0$, three cases arise:

(i) $h_1 > h_2$: $T_\times > 0$, and

$$T < T_\times : \ \rho_{\mathrm{L}} < \rho_{\mathrm{C}}(T), \qquad T = T_\times : \ \rho_{\mathrm{L}} = \rho_{\mathrm{C}}(T_\times), \qquad T > T_\times : \ \rho_{\mathrm{C}}(T) < \rho_{\mathrm{L}}.$$

(ii) $h_1 = h_2 = h$: $\rho_{\mathrm{L}} = 1$ and

$$\rho_{\mathrm{C}}(T) = \frac{-3T + |3T - 2h^2|}{2h^2} = \begin{cases} 1 - \dfrac{3T}{h^2}, & 0 \le T < \dfrac{2h^2}{3}, \\ -1, & T \ge \dfrac{2h^2}{3}, \end{cases}$$

hence $\rho_{\mathrm{C}}(T) \le 1 = \rho_{\mathrm{L}}$ for all $T > 0$.

(iii) $h_1 < h_2$: $T_\times < 0$, so for admissible $T > 0$ the equality $\rho_{\mathrm{C}}(T) = \rho_{\mathrm{L}}$ cannot be reached. Along the real branch of $\rho_{\mathrm{C}}(T)$ the dependence on T is continuous, and therefore, once $\rho_{\mathrm{C}}(T)$ drops below ρ_{L} for $T > 0$, the inequality $\rho_{\mathrm{C}}(T) < \rho_{\mathrm{L}}$ persists for all admissible $T > 0$. Since $\rho_{\mathrm{L}} = h_2^2/h_1^2 > 1$ while $\rho_{\mathrm{C}}(T) \le 1$ for small T, the inequality $\rho_{\mathrm{C}}(T) < \rho_{\mathrm{L}}$ holds for all $T > 0$.

For small capillarity ($T \longrightarrow 0$), a Taylor expansion of ρ_{C} yields

$$\rho_{\mathrm{C}}(T) = 1 - \frac{3T}{h_1 h_2} + O(T^2),$$

so the curve $\rho_{\mathrm{C}}(T)$ departs from unity with slope $-3/(h_1 h_2)$. Hence, for $h_1 > h_2$ the crossing $\rho_{\mathrm{C}}(T) = \rho_{\mathrm{L}} < 1$ occurs at a finite $T_\times > 0$, whereas for $h_1 \le h_2$ the ordering $\rho_{\mathrm{C}}(T) \le 1 \le \rho_{\mathrm{L}}$ is maintained even for arbitrarily small $T > 0$.

In the opposite, capillarity-dominated regime ($T \longrightarrow \infty$), the leading terms in formula (7) cancel, yielding the simple asymptotic limit

$$\rho_{\mathrm{C}}(T) = -\frac{h_2}{h_1} + O\left(\frac{1}{T}\right),$$

so that

$$\lim_{T\to\infty} \rho_{\mathrm{C}}(T) = -\frac{h_2}{h_1} < 0, \qquad \rho_{\mathrm{L}} = \frac{h_2^2}{h_1^2} \text{ is independent of } T.$$

Thus, for $h_2 \ge h_1$ one always has $\rho_{\mathrm{C}}(T) \le 1 \le \rho_{\mathrm{L}}$ throughout the entire range $T \ge 0$ along the real branch of $\rho_{\mathrm{C}}(T)$. For $h_2 < h_1$, the inequality eventually reverses once $T > T_\times$.

The analytical relations derived above show that the relative placement of ρ_{L} and $\rho_{\mathrm{C}}(T)$ at $k = 0$ depends on both geometry and surface tension: a positive threshold $T_\times$ satisfying $\rho_{\mathrm{C}}(T_\times) = \rho_{\mathrm{L}}$ exists only when $h_1 > h_2$. This behaviour underlies the long-wave topology of neutral-stability boundaries first noted by Grimshaw and Pullin [4], where the neutral curves separating focusing and defocusing regimes form closed contours in the (ρ, k) plane.

2.4. Long-wave critical surface tension T^* (Bond threshold Bo = 1/3)

To determine the long-wave threshold and introduce convenient notation, we define the Bond number $\mathrm{Bo} = T/h_1^2$ following the standard convention [24, 25]. The corresponding critical surface tension is

$$T^* = \frac{h_1^2}{3}, \tag{8}$$

which is equivalent to $\mathrm{Bo}^* = 1/3$ [6, 7]. This threshold separates the regimes of normal and anomalous dispersion in the long-wave limit: for $\mathrm{Bo} < \mathrm{Bo}^*$ ($T < T^*$) the small-k curvature $\omega''(k)$ is negative (normal dispersion), whereas for $\mathrm{Bo} > \mathrm{Bo}^*$ ($T > T^*$) it becomes positive (anomalous dispersion).

From the dispersion relation (1), in the limit of a light upper layer ($\rho \to 0$), corresponding to long gravity–capillary waves at the free surface of the lower layer, we obtain

$$\omega^2 = \frac{(1+Tk^2)\,k}{\coth(kh_1)} = (1+Tk^2)\,k\,\tanh(kh_1) = h_1k^2\Big[1 + \Big(\mathrm{Bo} - \tfrac{1}{3}\Big)(kh_1)^2 + O\Big((kh_1)^4\Big)\Big]\,.$$

Hence,

$$\omega(k) = \sqrt{h_1}\,k\Big[1 + \tfrac{1}{2}\Big(T - \tfrac{h_1^2}{3}\Big)k^2 + O(k^4)\Big]\,, \qquad \omega''(k) = 3\sqrt{h_1}\Big(T - \tfrac{h_1^2}{3}\Big)\,k + O(k^3).$$

At $T = T^*$ ($\mathrm{Bo} = \mathrm{Bo}^*$), the curvature $\omega''(k)$ vanishes, and the dispersion relation becomes degenerate. This is the classical long-wave, or shallow-water, threshold where the dispersive coefficient changes sign [6, 7].

The link between this linear threshold and the nonlinear modulation follows from the asymptotics of the Benjamin–Feir index (3). In the double limit $k \to 0$ and $\rho \to 0$ (long waves on a light upper layer),

$$\lim_{\rho\to 0}\lim_{k\to 0} J = \frac{9}{16\,h_1\,(-h_1^2 + 3T)},$$

so J diverges precisely at $T = T^*$, corresponding to $\mathrm{Bo} = \mathrm{Bo}^*$, in agreement with the long-wave shallow-water theory [6, 7]. At this value, the curves $J \to \infty$ and $\omega'' = 0$ intersect at the origin of the (ρ, k) plane: for $T < T^*$, the $J \to \infty$ branch is locally vertical, whereas for $T > T^*$ it becomes nearly horizontal. As T increases further, the curves $J \to \infty$ and $\omega'' = 0$ approach one another and nearly coincide, forming the degenerate "cut" structure observed in the modulational-stability diagrams.

2.5. Geometric condition for horizontal tangency of the critical surface

As shown in Subsec. 2.4, the long-wave Bond threshold $T^* = h_1^2/3$, $\mathrm{Bo}^* = 1/3$, marks the point where the singular conditions $J \to \infty$ and $\omega'' = 0$ coincide at $(\rho, k) = (0, 0)$. The geometry of the critical surface $T(\rho, k)$ near this point depends on the depth ratio of the layers.

Expanding the dispersion relation (1) for small k yields

$$\omega^2 = c_2(\rho)\,k^2 + c_4(\rho; T)\,k^4 + O(k^6),$$

with

$$c_2(\rho) = \frac{h_1h_2(1-\rho)}{h_1\rho + h_2}, \quad c_4(\rho;T) = \frac{h_1h_2\big[3T(h_1\rho + h_2) + h_1^2h_2(\rho - 1) + h_1h_2^2(\rho^2 - \rho)\big]}{3(h_1\rho + h_2)^2}.$$

The condition $c_4(\rho; T) = 0$ defines the critical surface-tension function

$$T^*(\rho) = \frac{h_1h_2\big(-h_1\rho + h_1 - h_2\rho^2 + h_2\rho\big)}{3(h_1\rho + h_2)}, \qquad T^*(0) = \frac{h_1^2}{3}.$$

In the long-wave limit, this degeneracy condition coincides with the singularity set $J \to \infty$; hence, the same function $T^*(\rho)$ locally describes both the linear dispersion surface $\omega'' = 0$ (green) and the nonlinear singular surface $J \to \infty$ (blue) in the vicinity of $(\rho, k) = (0, 0, T^*)$.

A horizontal tangency of $T(\rho, k)$ to the plane $T = T^*$ at $(\rho, k) = (0, 0)$ requires $\partial T^*/\partial\rho|_{\rho=0} = 0$, which gives

$$h_1^2 + h_2(h_1 - h_2) = 0, \qquad \frac{h_2}{h_1} = \frac{1+\sqrt{5}}{2} \approx 1.618. \tag{9}$$

Hence, the critical surface is horizontally tangent at the origin when the depth ratio satisfies (9). This ratio corresponds to the *golden ratio* $\varphi = (1+\sqrt{5})/2$, representing a neutral balance between the inertial contributions of the two layers in the long-wave limit. For $h_2/h_1 < \varphi$, $\partial T^*/\partial\rho|_{\rho=0} < 0$, indicating a gravity-dominated regime; for $h_2/h_1 > \varphi$, the derivative is positive, corresponding to a capillarity-dominated regime, while the golden-ratio configuration $h_2/h_1 = \varphi$ defines the boundary between these two regimes.In particular, when the depth ratio exceeds the golden value $h_2/h_1 = \varphi$ and the surface tension is increased beyond the long-wave threshold T^*, the resulting change in the local geometry of the critical surfaces $J \to \infty$ and $\omega'' = 0$ leads to a qualitative restructuring of the modulational-stability diagrams, as will be illustrated in Sec. 4.

3. STABILITY DIAGRAMS: THE INFLUENCE OF SURFACE TENSION

3.1. General remarks and reference configuration

In Part I, modulational–stability maps were constructed for two representative sets of layer–depth combinations, $(h_1, h_2) \in \{1, 2, 3, 4\}$ and $(h_1, h_2) \in \{1, 5, 9, 13\}$, which together illustrated the main topological types of stable and unstable regions and their evolution with varying density ratio ρ and wavenumber k. In the present part, attention is focused on the second, broader matrix $(h_1, h_2) \in \{1, 5, 9, 13\}$, which serves as a reference configuration for analysing the effect of surface tension. Other geometric and physical parameters of the system will be examined in the following subsections.

Figure 1 shows the modulational–stability diagrams for three representative values, $T = 1/2$, 1, and 2. The colour convention is the same as in Part I: black denotes the linear–stability boundary corresponding to the *critical wavenumber*

$$k = k_\mathrm{c} = \sqrt{(\rho - 1)/T},$$

which separates the regions of linear stability and instability; red indicates the curve $J = 0$ separating focusing and defocusing nonlinearities; blue marks the singular curve $J \longrightarrow \infty$ associated with resonance coupling; and green represents the dispersion–curvature line $\omega''(k) = 0$, where the sign of the group–velocity dispersion changes. Solid, dashed, and dotted lines correspond to $T = 1/2$, 1, and 2, respectively. This comparison highlights how an increase in surface tension gradually modifies the topology of stable and unstable domains across the parameter space (ρ, k).

3.2. Symmetric and asymmetric configurations of the upper unstable region

The influence of surface tension on the upper modulationally unstable domain (bounded above by the red locus $J = 0$) can be examined by comparing three representative values, $T = 1/2$ (solid), 1 (dashed), and 2 (dotted), across all panels of Fig. 1. As shown in Part I, deviations of T from the reference value $T = 1$ produce opposite yet comparable effects: doubling to $T = 2$ and halving to $T = 1/2$ deform the upper domain in reverse directions with nearly symmetric magnitudes.

For equal depths ($h_1 = h_2$), the upper region remains continuous at $\rho = 1$, without a vertical cut. In Fig. 1a ($h_1 = h_2 = 1$) the red boundaries for different T intersect twice, the left intersection occurring at relatively large wavenumbers ($k > 2$). For $\rho < 1$, the ordering of curves is dotted ($T = 2$) above dashed ($T = 1$) above solid ($T = 1/2$), indicating that increasing surface tension narrows the upper unstable domain, whereas decreasing T broadens it. This qualitative property persists along the diagonal of the matrix (Figs. 1f, k, p), where $h_1 = h_2 = h$: the asymptote at $\rho = 1$ does not appear, and the intersection point of the T-dependent boundaries shifts toward smaller k as h increases. The corresponding characteristic wavenumber

$$k_\mathrm{ch}(h) = \frac{1}{2h} \ln(9 + 4\sqrt{5}),$$

given by formula (5), decreases monotonically with h and approaches $(\rho, k) = (1, 0)$ in the deep–water limit, consistent with the case of two hydrodynamic half–spaces. As can be seen in the panels corresponding to the equal–depth configurations (Figs. 1a, f, k, p), the point $(\rho, k) = \big(1,\ k_\mathrm{ch}(h)\big)$ appears as the unique location at which all red boundaries ($J = 0$) corresponding to $T = 1/2$, 1, and 2 intersect. This common intersection is a distinctive geometric feature of the symmetric case $h_1 = h_2 = h$; for unequal layer depths such a point does not exist, and instead the line $\rho = 1$ becomes a vertical asymptote of the upper unstable region, as discussed below.

When depth symmetry is broken, the topology of the upper region changes at $\rho = 1$. In the first row of Fig. 1b–d ($h_1 = 1$, $h_2 > 1$), the intersection at $\rho = 1$ is replaced by a vertical asymptote that divides the upper domain, although the relative ordering of the T-dependent boundaries away from $\rho = 1$ remains similar to that in Fig. 1a. In contrast, Figs. 1e, i, m ($h_2 = 1$, $h_1 = 5, 9, 13$) exhibit a reversed response at small density ratios: the dotted curve ($T = 2$) lies below the dashed one ($T = 1$), while the solid curve ($T = 1/2$) lies above both, so increasing T expands the upper unstable domain and decreasing T contracts it. For larger ρ ($\rho \gtrsim 0.3$) this tendency reverses. In the remaining panels of Fig. 1 (rows 2–4, columns 2–4), the pairwise intersection points of the T-dependent boundaries cluster near $\rho \simeq 0.85$–0.99; within this range the order of curves is temporarily reversed, but just below $\rho = 1$ the usual sequence (dotted below dashed, solid above both) is restored.

The physical mechanism underlying these reorganizations is the redistribution of the balance between focusing and defocusing nonlinearities by capillarity under nearly fixed dispersion. The capillary contribution to the effective nonlinearity scales as $T\, k^5(1 - \rho)$: for a light upper layer ($\rho < 1$) an increase in T stiffens the interface and shifts the $J = 0$ boundary upward in k, narrowing the unstable region. Near and above density matching, particularly under pronounced depth asymmetry, the same increase in T can enhance the focusing component and expand the instability zone. Depth symmetry ($h_1 = h_2$) removes the singular response at $\rho = 1$, producing a smooth passage of the $J = 0$ locus across the density–matching line, whereas asymmetry restores a nearly singular sensitivity manifested as a vertical asymptote. The clustering of intersection points near $\rho \lesssim 1$ shows that, for small density contrast, variations in T mainly tune the high–k capillary stiffness without significantly changing the inertial balance between layers, leading to local, topology-preserving adjustments of the upper boundary rather than qualitative alterations of its shape.

3.3. Corridor and cut formation

The stability structures associated with the corridor and the cut, which represent additional stable regions, are absent in Fig. 1a for the symmetric case $h_1 = h_2 = 1$. In the subsequent panels (Figs. 1b–d) a narrow cut appears, terminating at both ends on the ρ-axis. For $h_1 = 1$ and $h_2 = 5$ only a single small cut is visible, corresponding to $T = 1/2$ (Fig. 1b).

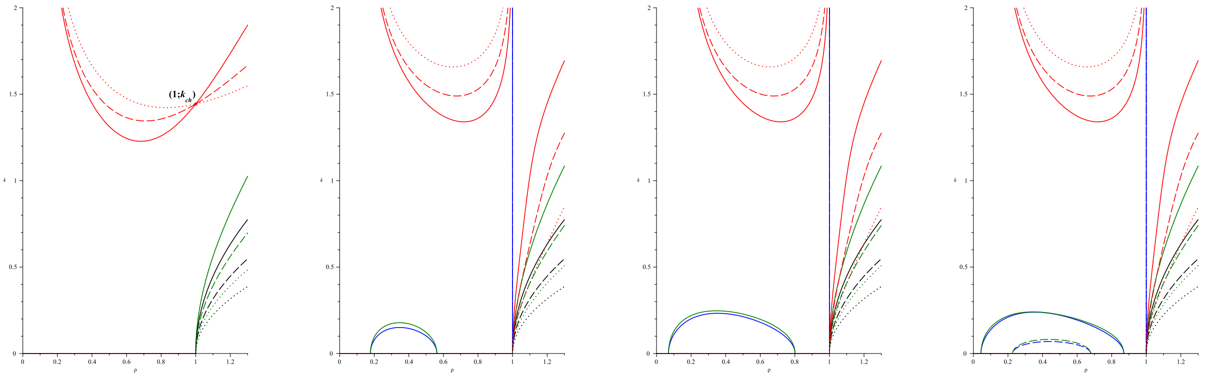

(a) $h_1 = 1,\ h_2 = 1$ **(b)** $h_1 = 1,\ h_2 = 5$ **(c)** $h_1 = 1,\ h_2 = 9$ **(d)** $h_1 = 1,\ h_2 = 13$

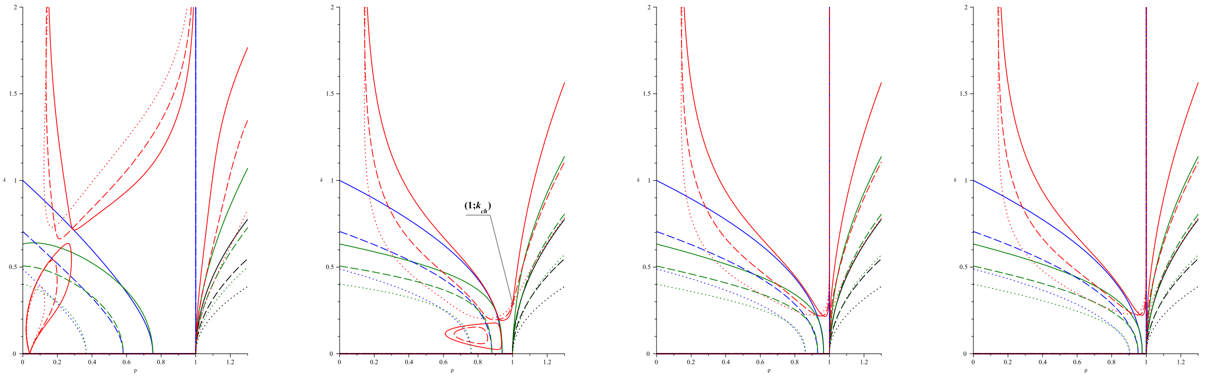

(e) $h_1 = 5,\ h_2 = 1$ **(f)** $h_1 = 5,\ h_2 = 5$ **(g)** $h_1 = 5,\ h_2 = 9$ **(h)** $h_1 = 5,\ h_2 = 13$

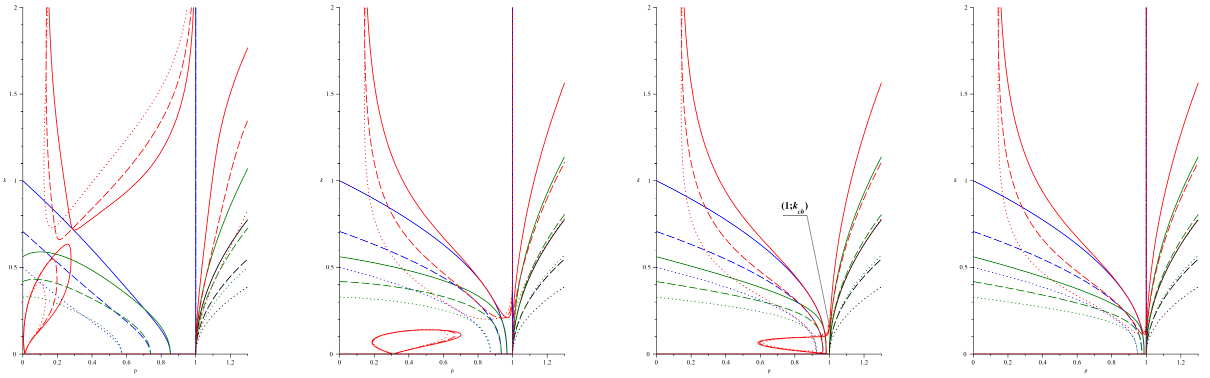

(i) $h_1 = 9,\ h_2 = 1$ **(j)** $h_1 = 9,\ h_2 = 5$ **(k)** $h_1 = 9,\ h_2 = 9$ **(l)** $h_1 = 9,\ h_2 = 13$

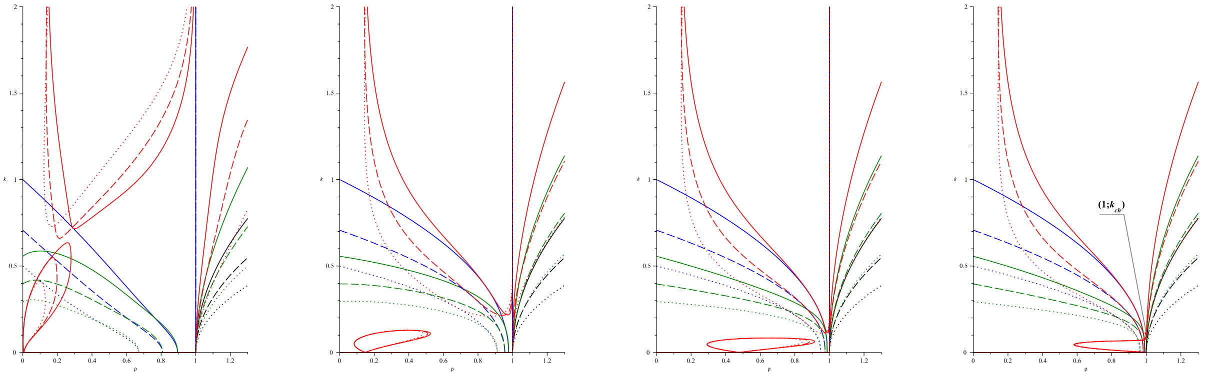

(m) $h_1 = 13,\ h_2 = 1$ **(n)** $h_1 = 13,\ h_2 = 5$ **(o)** $h_1 = 13,\ h_2 = 9$ **(p)** $h_1 = 13,\ h_2 = 13$

Figure 1. Modulational–stability diagrams for all combinations of $h_1, h_2 \in \{1, 5, 9, 13\}$ for $T = 1/2, 1, 2$.

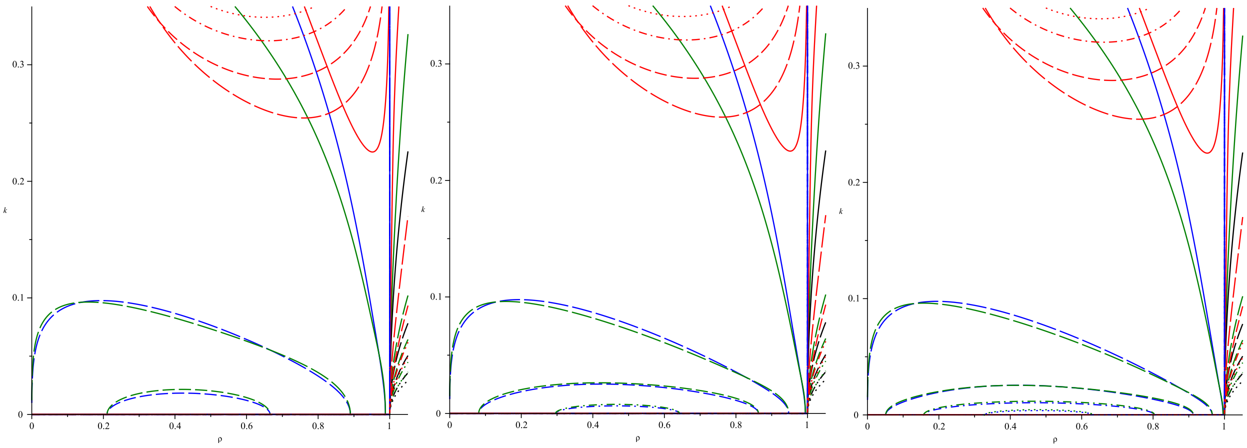

(a) $h_1 = 5,\ h_2 = 50$ **(b)** $h_1 = 5,\ h_2 = 100$ **(c)** $h_1 = 5,\ h_2 = 150$

Figure 2. The cut-type corridor for $h_1 = 5$ and $h_2 \in \{50, 100, 150\}$ for $T = 1,\ 25/3,\ 20,\ 40,\ 60$.

When the upper-layer thickness increases to $h_2 = 9$, the cut persists for $T = 1/2$, becomes noticeably longer, and extends to higher wavenumbers (Fig. 1c). At $h_2 = 13$ (Fig. 1d), two distinct cuts are observed: a broader one associated with $T = 1/2$ and a smaller one corresponding to $T = 1$.

At significantly higher depth ratios, the narrow cuts characteristic of moderate asymmetry transform into broad open corridors. This behaviour is consistent with the analytical result of Subsec. 2.5, which shows that the critical surface $T^*(\rho)$ develops a horizontal tangency at $(\rho, k) = (0, 0)$ when the depth ratio satisfies $h_2/h_1 = (1 + \sqrt{5})/2 \approx 1.618$. For depth ratios exceeding this value, the local geometry of the critical surfaces $J \longrightarrow \infty$ and $\omega'' = 0$ changes in such a way that cut–type structures naturally emerge: in this regime the singular branch $J \longrightarrow \infty$ bends toward the $k = 0$ axis, producing cuts that visibly rest on the ρ–axis. This effect is clearly seen in the moderately asymmetric panels of Fig. 1b–d and becomes even more transparent in the three–dimensional representations discussed in Sec. 4.

For $h_1 = 5$ and $h_2 = 50$, 100, and 150 (Figs. 2a–c), several distinct corridors are observed, their structure depending on the magnitude of surface tension ($T = 1$, 25/3, 20, 40, and 60), represented by solid, long-dashed, dashed, dash-dotted, and dotted lines, respectively. The chosen five values of T play a key methodological role. They cover the reference case $T = 1$ used throughout Part I, the critical long-wave threshold (8)

$$T^* = \frac{h_1^2}{3} = \frac{25}{3}, \qquad \mathrm{Bo}^* = \frac{1}{3},$$

and three progressively higher values $T = 20, 40$, and 60, which extend the analysis well into the strongly capillary regime. This set allows one to track, within a single series of diagrams, the complete transition from gravity–capillary balance to capillary dominance and to identify the scaling of corridor width, shape, and position with increasing T.

For $h_2 = 50$ (Fig. 2a) only three corridors are present ($T = 1$, 25/3, and 20); for $h_2 = 100$ (Fig. 2b) four corridors appear ($T = 1$, 25/3, 20, 40); and for $h_2 = 150$ (Fig. 2c) all five corridors corresponding to $T = 1$, 25/3, 20, 40, and 60 are clearly visible. At $T = 1$ the corridor remains broad and nearly invariant with h_2, while increasing T primarily affects the region of small k, where pronounced cuts develop in the central part of the ρ-range. As T exceeds the critical value T^*, the individual corridors converge toward the origin $(\rho, k) = (0, 0)$, producing a cut-type topology.

This behaviour marks the transition from a mixed gravity–capillary regime to a purely capillary one. For moderate surface tension ($T < T^*$), both restoring mechanisms act simultaneously, producing multiple corridors whose positions depend on the density ratio. As T approaches T^*, the capillary stress increasingly dominates, damping long-wave modulation and localizing the instability at short wavelengths. The cut-type corridor thus corresponds to the limit in which the interface behaves as a nearly rigid capillary sheet bounding a deep lower layer: nonlinear effects persist only within a narrow density interval, and the unstable band detaches from the ρ-axis. In this regime, the inertia of the lower layer provides the dominant response, while dispersion is governed exclusively by surface tension, resulting in the flattening and eventual disappearance of the loop.

3.4. Loop and its interaction with the corridor

From the second (Figs. 1e–h), third (Figs. 1i–l), and fourth (Figs. 1m–p) rows of the matrix diagrams corresponding to $h_1 = 5$, 9, and 13, respectively, it is seen that at a lower value of surface tension ($T = 1/2$) both stability structures—the loop and the corridor—expand relative to the reference case $T = 1$, while the corridor shifts rightward along the ρ-axis. Its lower boundary, however, never crosses the line $\rho = 1$, approaching the point $(\rho, k) = (1, 0)$ asymptotically as the upper–layer thickness increases. At a higher value of surface tension ($T = 2$), both the loop and the corridor contract and become narrower, and the corridor moves leftward toward smaller density ratios. In the complete matrix of stability maps (Fig. 1), the loop is observed in Figs. 1e, f, i–k, m–p; in Fig. 1f it remains isolated, whereas in the other cases it touches the ρ-axis.

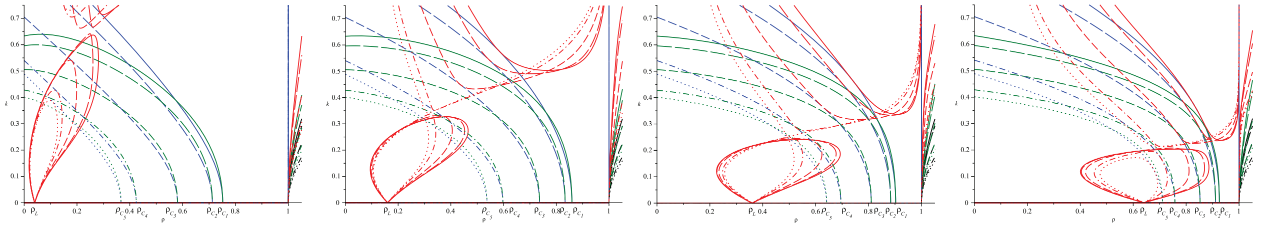

(a) $h_1 = 5,\ h_2 = 1$ **(b)** $h_1 = 5,\ h_2 = 2$ **(c)** $h_1 = 5,\ h_2 = 3$ **(d)** $h_1 = 5,\ h_2 = 4$

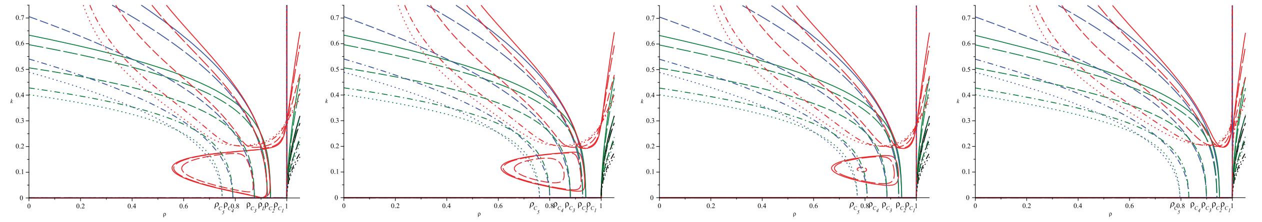

(e) $h_1 = 5,\ h_2 = 4.75$ **(f)** $h_1 = 5,\ h_2 = 5$ **(g)** $h_1 = 5,\ h_2 = 5.25$ **(h)** $h_1 = 5,\ h_2 = 6$

Figure 3. Stability diagrams for surface–tension coefficients $T = 1/2,\ 3/5,\ 1,\ 5/3,\ 2$ for $h_1 = 5$ and $h_2 \in \{1, 2, 3, 4, 4.75, 5, 5.25, 6\}$.

Figure 3 presents enlarged fragments of the modulational–stability maps for fixed $h_1 = 5$ and a sequence of upper–layer thicknesses $h_2 = 1, 2, 3, 4, 4.75, 5, 5.25, 6$ (Figs. 3a–h), computed for five values of surface tension, $T = 1/2$, $3/5$, 1, $5/3$, and 2, represented by solid, long-dashed, dashed, dash-dotted, and dotted lines. Each panel shows the relative configuration of the loop and the corridor near small wavenumbers k, illustrating how their positions vary with both geometry and surface tension. The loop–base point at $k = 0$ is determined solely by the depth ratio, $\rho_L = h_2^2/h_1^2$, whereas the corridor–edge points ρ_{C_1}–ρ_{C_5} correspond to these five values of T and mark the roots of the corridor branches on the horizontal axis, that is, the intersections of the resonant ($J \to \infty$) and dispersive ($\omega'' = 0$) conditions at $k \to 0$.

For quantitative reference, the corresponding values of ρ_L and $\rho_C(T)$ are summarized in Table 1.

Table 1. Loop–base ρ_L and corridor–edge $\rho_C(T)$ coordinates for five representative surface–tension values at fixed $h_1 = 5$.

h_2	ρ_L	$\rho_{C_1} = \rho_C(1/2)$	$\rho_{C_2} = \rho_C(3/5)$	$\rho_{C_3} = \rho_C(1)$	$\rho_{C_4} = \rho_C(5/3)$	$\rho_{C_5} = \rho_C(2)$
1.00	0.040	0.752	0.712	0.580	0.424	0.367
2.00	0.160	0.859	0.833	0.737	0.597	0.537
3.00	0.360	0.903	0.884	0.810	0.695	0.641
4.00	0.640	0.926	0.911	0.853	0.758	0.711
4.75	0.902	0.937	0.924	0.874	0.791	0.749
5.00	1.000	0.940	0.928	0.880	0.800	0.760
5.25	1.103	0.943	0.931	0.885	0.809	0.770
6.00	1.440	0.950	0.940	0.899	0.831	0.796

The inclusion of the loop–base coordinate ρ_L in Fig. 3 clarifies the mutual placement of the loop and corridor edge points. For all configurations, the corridor–edge coordinate $\rho_C(T)$ (corresponding to ρ_{C_1}–ρ_{C_5} in Table 1) decreases monotonically with increasing T. When $h_2 < h_1$, the values $\rho_C(T)$ lie strictly above the loop base ρ_L and approach it from the right as T increases, indicating a gradual contraction of the corridor toward the loop. In contrast, when $h_2 > h_1$, the quantities $\rho_C(T)$ remain strictly below unity and therefore stay well separated from the loop–base coordinate $\rho_L > 1$ for all admissible values of T. In this regime, the loop and corridor bases do not approach one another as the surface tension varies; instead, their persistent separation reflects the dominance of geometric asymmetry over the capillary adjustment of the resonant and dispersive branches.

As shown in Figs. 3(a–d), for $h_2 = 1$–4 the loop–base coordinate $\rho_L = h_2^2/25$ remains considerably smaller than the corresponding corridor–edge values ρ_{C_1}–ρ_{C_5} for all surface–tension magnitudes listed in Table 1. Hence, the corridor always originates to the right of the loop base, satisfying $\rho_C(T) > \rho_L$. At small surface tension ($T = 1/2$) the corridor widens and its right edge extends well beyond ρ_L, forming a broad composite loop–corridor domain. As T increases, the corridor contracts and shifts leftward as $\rho_C(T)$ approaches ρ_L, and the loop correspondingly narrows. In the most asymmetric case ($h_2 = 1$) the loop remains detached from the ρ-axis, whereas for $h_2 = 2$–4 it touches the $O\rho$-axis and gradually enlarges with increasing h_2. This behaviour indicates that a thicker upper layer increases the effective inertia above the interface, thereby strengthening the dispersive response and widening the interval of nonlinear–dispersive balance at small k.

Fig. 3e corresponds to nearly symmetric configurations ($h_2 \simeq h_1$), where the loop–base point ρ_L approaches unity and the corridor–edge coordinates ρ_{C_i} $(i = 1-5)$ remain slightly below 1 for all values of T. For $h_2 = 4.75$, one finds $\rho_L = 0.903$ and $\rho_{C_1} = 0.937$, indicating that at small T the corridor begins slightly to the right of the loop base, forming a large loop resting on the ρ-axis. As surface tension increases, the edge positions ρ_{C_i} shift left of ρ_L (e.g., for $T = 2$, $\rho_{C_5} = 0.749$), and the loop contracts. In the fully symmetric case $h_2 = 5$ (Fig. 3f), where $\rho_L = 1$ and all $\rho_{C_i} < 1$, no vertical asymptote appears at $\rho = 1$, and the loop always rests on the ρ-axis at $(1, 0)$. The corridor base lies to the left of this point and moves further left as T increases, showing that decreasing surface tension enlarges the corridor and enhances its overlap with the loop, whereas higher T suppresses this interaction. The convergence of ρ_L and ρ_{C_i} toward unity with increasing total depth explains the near coincidence of the loop and corridor bases in these quasi–symmetric configurations.

For $h_2 > h_1$ (Figs. 3(g, h)), the loop–base coordinate satisfies $\rho_L > 1$, while $\rho_{C_i} < 1$ for all T (see Table 1). Thus, the corridor originates to the left of the loop base, and their interaction depends on whether the corridor's right boundary at finite k extends beyond ρ_L. For slightly asymmetric configurations (h_2 close to h_1; Fig. 3(g)), this occurs only at small T, when ρ_{C_1} is closest to unity and the corridor is widest; under these conditions the loop persists in a degenerate form without reaching the ρ-axis. As the upper layer becomes thicker (h_2 further increases; Fig. 3(h)), even such degenerate loops no longer appear, and only the corridor structure remains.

These geometric dependences outline the quantitative trends governing the interaction between the loop and the corridor under varying surface tension. The corresponding physical interpretation is summarized in Sec. 3.5.

3.5. Summary and physical interpretation

The contrasting effects of surface tension in the two limiting geometries— loop formation in the HS–La system and cut development in the La–HS system— previously described in [27, 28], are consistently reproduced within the present unified two-layer framework. When the upper layer becomes thicker than the lower one, the interfacial mode acquires a predominantly capillary character: the restoring force is governed by surface tension rather than gravity, and increasing T enhances this dominance, narrowing the parameter range in which nonlinearity and dispersion compensate. Consequently, the loop shrinks and may disappear, leaving only the narrow stability corridor.

The joint analysis of ρ_L and $\rho_C(T)$ clarifies the structural transitions observed in Fig. 3. For $h_2 < h_1$ and small T, the corridor begins to the right of the loop base ($\rho_C(T) > \rho_L$), so that the loop lies entirely beneath the corridor in the (ρ, k)-plane. As T increases at fixed geometry ($h_2 < h_1$), the value $\rho_C(T)$ decreases monotonically, and the corridor correspondingly shifts leftward along the ρ-axis. When $\rho_C(T)$ drops below ρ_L (at $T = T_\times$; see Sec. 2.3), the loop ceases to exist and only the corridor remains. When $h_2 \geq h_1$, the condition $\rho_C(T) = \rho_L$ has no solution for any admissible $T > 0$, and the loop is absent for all surface–tension magnitudes.

Surface tension thus controls the relative positioning of the loop and corridor at small wavenumbers: decreasing T moves the corridor to the right and allows a loop to exist beneath it, whereas increasing T shifts the corridor leftward and eliminates the loop. In the symmetric geometric limit $h_2 \to h_1$ one has $\rho_L \to 1$, while for $T \to 0$ one obtains $\rho_C(T) \to 1^-$, so that both base points accumulate near the long–wave limiting point $(\rho, k) = (1, 0)$. In the additional deep–water limit $h_1, h_2 \to \infty$, this configuration approaches the classical model of two hydrodynamic half–spaces.

A three–dimensional perspective of these transitions is presented in Sec. 4, which shows how loops, corridors, and cuts merge or collapse as the surface–tension magnitude and the depth ratio h_2/h_1 increase.

4. THREE-DIMENSIONAL CRITICAL SURFACES $T(\rho, k)$

4.1. Analytical framework and Bond-threshold structure

A comprehensive understanding of the modulational–stability topology can be achieved by extending the two-dimensional maps of Sec. 3 into the full three-dimensional parameter space (ρ, k, T). The stability diagrams discussed earlier represent planar sections of this space at fixed T, showing how the upper stability region, the corridor, and the loop transform as the surface–tension coefficient varies. In three dimensions these structures arise from the three continuous critical surfaces defined by

$$J(\rho, k; h_1, h_2, T) = 0, \qquad J(\rho, k; h_1, h_2, T) \to \infty, \qquad \omega''(\rho, k; h_1, h_2, T) = 0,$$

and from their mutual arrangement in the (ρ, k, T) space. The first surface ($J = 0$, red) separates focusing and defocusing nonlinearities, the second ($J \to \infty$, blue) corresponds to the resonant singularity, and the third surface ($\omega'' = 0$, green) marks the change of sign of group–velocity dispersion. Taken together, these three critical surfaces provide the geometric framework for the three–dimensional organisation of modulationally stable and unstable regions in the (ρ, k, T) space.

It is useful to distinguish between the long-wave critical value of surface tension and the full three-dimensional critical structure. The Bond threshold T^* is a scalar quantity: it specifies the value of T at which the curvature ω'' vanishes in the limit $k \longrightarrow 0$, marking the transition between gravity- and capillarity-dominated dispersion. In contrast, the critical conditions $\omega'' = 0$ and $J \longrightarrow \infty$ define two distinct two-dimensional surfaces in the (ρ, k, T) space. Their planar sections at fixed T give the neutral-stability curves that delimit modulationally stable and unstable regions in the (ρ, k) plane.

According to expression (8) in Subsec. 2.4, the long-wave Bond threshold $T^* = h_1^2/3$ (with $\mathrm{Bo}^* = 1/3$) is the unique value at which the long-wave limits of the resonant condition $J \longrightarrow \infty$ and the dispersive condition $\omega'' = 0$ coincide at the point $(\rho, k) = (0, 0)$. In the three-dimensional space (ρ, k, T) this point lies on a one-dimensional intersection curve (a nodal line) along which the resonant (blue) and dispersive (green) surfaces meet.

Although the resonant and dispersive critical surfaces intersect along a one-dimensional curve and lie geometrically close to each other over wide regions of the (ρ, k) plane for many depth configurations, their local behaviour near $(\rho, k) = (0, 0)$ remains distinct for all $T < T^*$. At the Bond-critical value $T = T^*$, the two surfaces exhibit a local degeneracy at $(\rho, k) = (0, 0)$, where they meet at the same height and have a common tangent. For $T > T^*$, planar sections $T =$ const intersect the two surfaces in a different manner, producing cut-type configurations; their detailed geometry will be discussed in Secs. 4.2–4.3.

In addition to the Bond threshold T^*, a second geometric degeneracy is associated with the depth ratio. As shown in Subsec. 2.5, the dispersive critical surface $T_{\omega''=0}(\rho, k)$ has a horizontal tangent at $(\rho, k, T) = (0, 0, T^*)$ when the layer depths satisfy the golden–ratio relation $h_2/h_1 = \varphi$. The consequences of this local geometric condition become evident in the three–dimensional structure discussed in Subsec. 4.2, where its impact on the critical surfaces is examined in detail.

4.2. Geometry of the critical surfaces and symmetry effects

Figure 4 shows the critical surfaces for the fixed lower-layer depth $h_1 = 5$ and a sequence of upper-layer thicknesses $h_2 \in \{1, 4, 5, 6, 5(1 + \sqrt{5})/2, 12, 50, 100, 150\}$. This set spans the transition from configurations with a thin upper layer to those in which the upper layer is effectively deep.

For $h_2 = 1$, the system is close to the HS–La limiting configuration, and the nonlinear surface $J = 0$ forms a pronounced loop near the origin [27]. The case $h_2 = 4$ represents moderate asymmetry, whereas $h_2 = 5$ gives the symmetric configuration discussed in Subsec. 2.2. Increasing the upper-layer thickness to $h_2 = 6$ introduces weak asymmetry. The value $h_2 = 5(1 + \sqrt{5})/2$ realises the golden–ratio depth ratio, at which both the dispersive ($\omega'' = 0$) and the resonant ($J \longrightarrow \infty$) critical surfaces acquire a horizontal tangent at $(\rho, k, T) = (0, 0, T^*)$; see Subsec. 2.5. Larger values $h_2 = 12, 50, 100, 150$ correspond to progressively deeper upper layers and bring the system close to the La–HS regime, in which the dispersive (green) and resonant (blue) surfaces lie geometrically close over a wide region of the (ρ, k) domain (see Subsec. 3.3 and [28]).

In every panel the point $(\rho, k, T) = (0, 0, T^*)$ appears as the intersection of the dispersive ($\omega'' = 0$) and resonant ($J \longrightarrow \infty$) surfaces. For $h_1 = 5$, its height is $T^* = 25/3$, in agreement with the analytic Bond threshold $T^* = h_1^2/3$ obtained in Subsec. 2.4.

In panels (a)–(f) of Fig. 4 the axes are scaled identically, which facilitates comparison of curvature and elevation. Panels (g)–(i) use an enlarged vertical scale that highlights the geometry of the critical surfaces for large values of h_2. These three-dimensional plots directly extend the detailed two-dimensional sections shown in Fig. 2 and analysed in Subsec. 3.3. In particular, the configurations with $h_2 = 50$, 100, and 150 correspond to planar diagrams in which three, four, and five cut-type corridors are present for the respective subsets of the surface-tension values $T = \{1,\ 25/3,\ 20\}$, $T = \{1,\ 25/3,\ 20,\ 40\}$, $T = \{1,\ 25/3,\ 20,\ 40,\ 60\}$. The three-dimensional representation thus visualises how these cut-type structures arise as intersections of the resonant ($J \longrightarrow \infty$) and dispersive ($\omega'' = 0$) critical surfaces at the corresponding T-levels.

For small and moderate asymmetry (Figs. 4a–d), the red surface $J = 0$ forms a convex sheet that rises above the (ρ, k)-plane at small T, while the blue and green critical surfaces remain well separated. Sections at fixed T reproduce the loop– and corridor–type structures identified in the two-dimensional matrix of Subsec. 3.2. The closed intersections of $J = 0$ give the loop-type stability islands, whereas the region lying between the resonant ($J \longrightarrow \infty$) and dispersive ($\omega'' = 0$) surfaces forms the open corridor that separates the low–k and high–k instability zones. Thus, in the regime of weak asymmetry these three-dimensional surfaces provide direct extensions of the characteristic curves forming the upper unstable region and the corridor in the planar diagrams of Subsecs. 3.2–3.4.

In panels (a)–(c) of Fig. 4, a grey horizontal plane marks the level $T = T_\times$ introduced in Subsec. 2.3. This plane intersects the upper part of the red surface $J = 0$ and separates the parameter ranges in which the loop has a well-defined base ($T < T_\times$) from those in which the loop becomes degenerate ($T > T_\times$), as illustrated in Fig. 3. For $h_2 = 1$ (panel (a)) and $h_2 = 4$ (panel (b)) the level $T_\times$ is positive and lies above most of the plotted region. In the symmetric case $h_2 = h_1 = 5$ (panel (c)) one has $T_\times = 0$, so the plane coincides with the coordinate plane $T = 0$. For $h_2 = 6$ (panel (d)), $T_\times < 0$, and the corresponding horizontal plane lies outside the plotted domain and is therefore not shown. A distant branch of the same red surface $J = 0$ is also visible in all panels of Fig. 4 as the remote background sheet forming the rear boundary of the three-dimensional plots. This rear branch exhibits its most noticeable deformation for small upper-layer

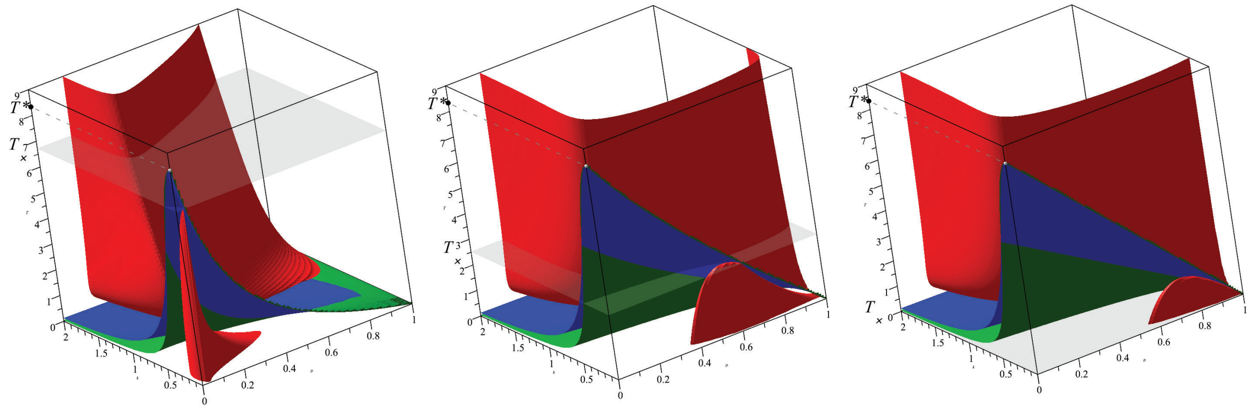

(a) $h_1 = 5,\ h_2 = 1$ **(b)** $h_1 = 5,\ h_2 = 4$ **(c)** $h_1 = 5,\ h_2 = 5$

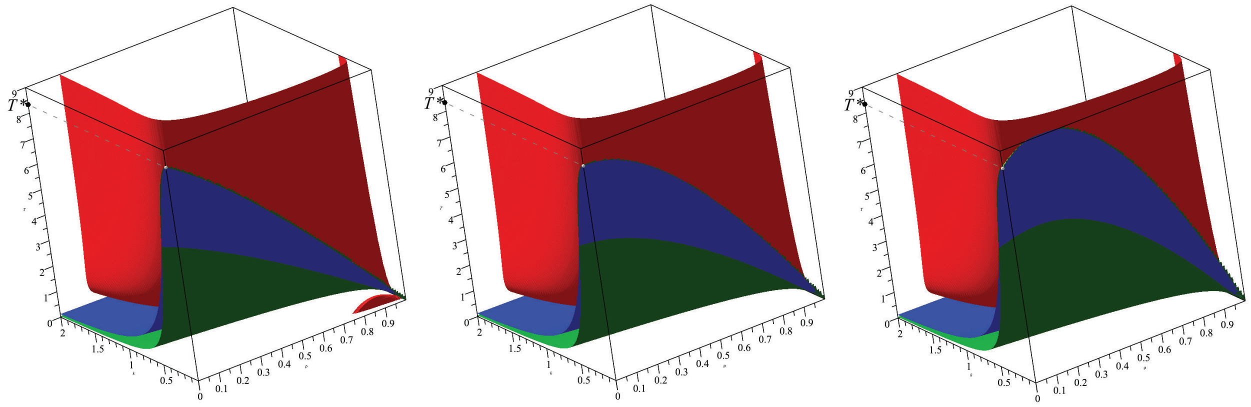

(d) $h_1 = 5,\ h_2 = 6$ **(e)** $h_1 = 5,\ h_2 = 5(1+\sqrt{5})/2 \approx 8.09$ **(f)** $h_1 = 5,\ h_2 = 12$

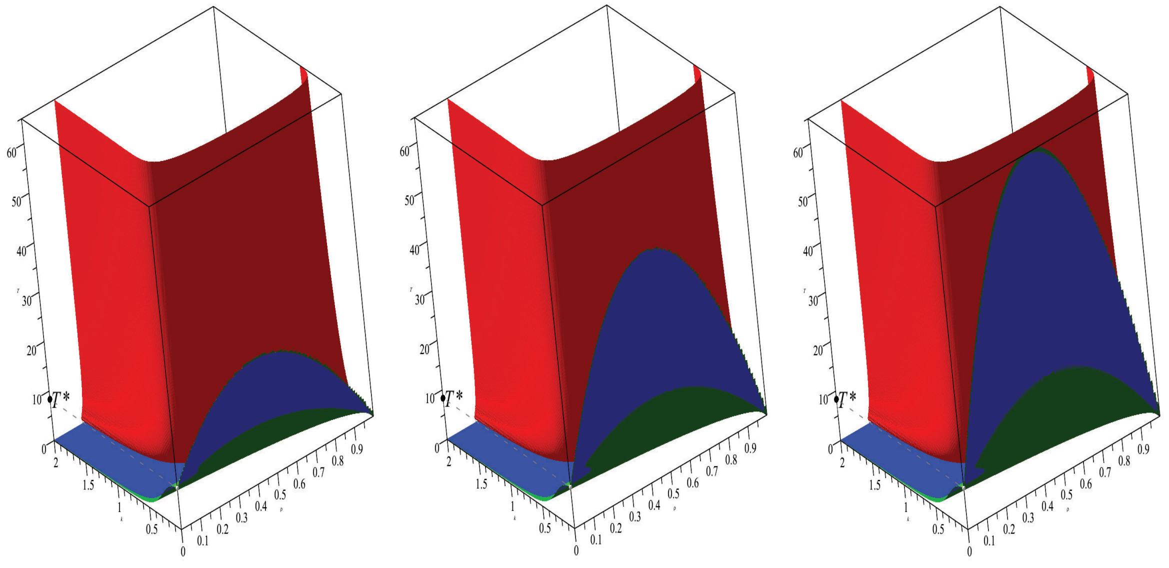

(g) $h_1 = 5,\ h_2 = 50$ **(h)** $h_1 = 5,\ h_2 = 100$ **(i)** $h_1 = 5,\ h_2 = 150$

Figure 4. Critical surfaces $T(\rho, k)$ for $h_1 = 5$ and $h_2 \in \{1, 4, 5, 6, 5(1+\sqrt{5})/2, 12, 50, 100, 150\}$.

depths: from panel (a) to panel (c) it gradually straightens, its curvature weakens, and the sheet approaches a more vertical orientation. For larger depth ratios $h_2 \geq h_1$, the subsequent changes of this background branch become smooth and relatively small; although the surface continues to deform as h_2 increases, the scale and perspective of the visualisation make these variations barely discernible in panels (d)–(i). Consequently, at large asymmetry the apparent geometry of this rear part of the red surface remains nearly unchanged, and the qualitative transformations of the modulational-stability topology are governed almost entirely by the behaviour of the blue and green surfaces.

In the vicinity of the level $T = T^*$, the singular surfaces $J \longrightarrow \infty$ (blue) and $\omega'' = 0$ (green) lie geometrically close to each other and intersect along a one–dimensional curve in the three–dimensional (ρ, k, T) space. The point $(\rho, k, T) = (0, 0, T^*)$ is the lower endpoint of this curve and corresponds to the coincidence of the long–wave dispersive and nonlinear singularities. The geometry of the intersection line, as well as the shape of the adjacent upper parts of the blue and green surfaces, depends sensitively on the depth ratio h_2/h_1. For $h_2 < h_1$ the two surfaces bend downward near $(0, 0, T^*)$, giving a visibly concave intersection line (panels (a), (b)). In the symmetric case $h_2 = h_1 = 5$ (panel (c)) the intersection line becomes nearly straight, reflecting the even symmetry of the dispersive characteristics with respect to k. For $h_2 > h_1$ the line bends upward, producing a convex shape, as seen beginning from panel (d).

As h_2 increases further, the upward bending of the resonant ($J \longrightarrow \infty$) and dispersive ($\omega'' = 0$) surfaces becomes more pronounced. At the golden–ratio depth ratio $h_2 = h_1(1 + \sqrt{5})/2$ (panel (e)), the common intersection line of the blue and green surfaces develops a horizontal tangent at the point $(\rho, k, T) = (0, 0, T^*)$, in agreement with the analytical condition of Subsec. 2.5. For $h_2 > h_1(1 + \sqrt{5})/2$, both surfaces acquire a distinct local maximum in their upper parts near small k; the same local maximum appears on their intersection line, as clearly visible in panels (f)–(i). This local extremum forces the intersection line to bend further upward in T, and its projections onto the planes $T = \text{const}$ give rise to the cut–corridor patterns described in Subsec. 3.3. In the two–dimensional stability diagrams, the intersection points of the cut boundaries correspond precisely to the projection of this three–dimensional blue–green intersection curve onto the (ρ, k) plane.

Overall, the evolution in panels (a)–(i) shows that the topological transitions in the (ρ, k)-plane are governed primarily by the geometry of the intersection line between the resonant ($J \longrightarrow \infty$) and dispersive ($\omega'' = 0$) surfaces. For small and moderate depth ratios h_2/h_1 this line is concave or nearly straight, producing corridor–type structures, while the loop is generated independently by the front branch of the $J = 0$ surface. Once h_2 exceeds the golden–ratio value, a local maximum emerges on the upper parts of the blue and green surfaces and on their intersection line, causing it to bend upward; its projections onto $T = \text{const}$ planes then yield the characteristic cut–corridor patterns of Subsec. 3.3. Thus, the deformation of this intersection line provides the geometric link between the gravity–capillary and capillary regimes of modulational stability.

4.3. Physical interpretation and correspondence with planar maps

The red surface $J = 0$ marks the boundary between the two signs of the nonlinear NLS coefficient and therefore separates the focusing and defocusing regimes. Its geometry shows how sensitively the nonlinear response of the interface depends on the density ratio and the wavenumber. The front part of this surface, clearly visible in the three–dimensional plots, generates a closed intersection with constant–T planes, producing the loop observed in the planar diagrams. As the upper layer becomes thicker, the gravitational contribution to nonlinearity is increasingly masked by the inertia of the upper fluid, so that the capillary term in J becomes dominant. In this regime the variation of J with respect to ρ becomes much weaker, the $J = 0$ surface straightens in the ρ–direction and shifts toward larger density ratios, and the resulting loop progressively shrinks and eventually disappears.

The blue surface, corresponding to the near–resonant nonlinear response ($J \longrightarrow \infty$), and the green surface associated with the change of sign of the group–velocity dispersion ($\omega'' = 0$), intersect along a one–dimensional curve that exists for all depth ratios. The mutual arrangement of these two surfaces, however, depends strongly on the ratio h_2/h_1. When the upper layer is thinner than the lower one, or only slightly thicker so that the depths remain comparable, the blue–green intersection line lies close to the density–matching region $\rho \simeq 1$. Away from this neighbourhood the surfaces separate, and their planar sections at fixed T produce two distinct branches whose projections bound a finite interval in ρ; this interval appears in the (ρ, k) plane as the *corridor*.

When the upper layer becomes much thicker than the lower one, the geometry changes qualitatively. For surface–tension magnitudes exceeding the long–wave threshold T^*, the upper parts of the blue and green surfaces rise in such a way that the projections of their intersection line onto the planes $T = \text{const}$ no longer bound a finite interval. In these sections the corridor collapses into a *cut*, which appears as a narrow band rooted at $k = 0$ and produced by the close proximity of the two critical surfaces in the three–dimensional geometry.

The curvature of the intersection line between the surfaces $J \longrightarrow \infty$ and $\omega'' = 0$ in the neighbourhood of $k = 0$ is governed by the long–wave distribution of inertia between the two layers and therefore by the depth ratio. When the lower layer is thicker ($h_2 < h_1$), most of the inertial mass resides in the lower fluid and the dynamical influence of the upper layer is weak. As the density ratio varies, the resonant nonlinear and dispersive mechanisms shift in different directions, and the long–wave portion of the intersection line acquires a downward concavity ($\bigcap$-shape), as seen in panels (a)–(b) of Fig. 4. In the symmetric configuration $h_2 = h_1$, the inertial contributions of the two layers become equivalent; in the long–wave limit the interface behaves as a single fluid column, and the response of the conditions $J \longrightarrow \infty$ and $\omega'' = 0$ to variations in ρ is nearly synchronised. As a result, the intersection line becomes approximately straight, as in panel (c). When the upper layer is thicker ($h_2 > h_1$), the inertial dominance reverses and the upper fluid governs the long–wave dynamics. The resonant and dispersive conditions then diverge in the opposite sense as ρ varies, and the intersection line becomes upward–concave ($\bigcup$-shape), as seen in panels (d)–(i). Thus, the change of convexity of the intersection line captures the transition from lower–layer dominance (downward concavity), through the symmetric regime (straight line), to upper–layer dominance (upward concavity).

The golden–ratio depth ratio $h_2/h_1 = \varphi$ does not by itself produce a cut. Rather, it marks the point at which the curvature of the blue–green intersection line changes sign and a horizontal tangent appears at $(\rho, k, T) = (0, 0, T^*)$. Only for depth ratios exceeding φ can a genuine local maximum develop on this line. As h_2 increases further, this maximum rises in T, and once it exceeds the level of a given plane $T = \text{const}$, the planar section exhibits a cut rooted at $k = 0$. This explains why cut–type structures appear only for sufficiently large h_2 (e.g. $h_2 = 12, 50, 100, 150$), even though the change of curvature originates at the golden–ratio configuration.

Thus, the loop, corridor, and cut correspond to three distinct physical–geometric regimes. The loop reflects a local balance between nonlinearity and dispersion. The corridor arises from a gentle separation between the resonant and dispersive mechanisms, produced when the corresponding critical surfaces remain well apart. The cut appears only when these two mechanisms become locally nearly simultaneous: for sufficiently large depth ratios and surface–tension magnitudes, the resonant and dispersive surfaces approach each other so closely that the intermediate region collapses into a narrow cut–type band rooted at $k = 0$.

5. CONCLUSIONS

Together with Part I, this study provides a unified geometric and asymptotic description of the modulational stability of interfacial gravity–capillary waves in a two-layer fluid. Treating the surface tension T as an independent control parameter reveals how capillarity modifies both the nonlinear coefficient J and the curvature of the dispersion relation ω'', and how these changes reorganise the neutral boundaries in the (ρ, k)–plane.

In the long-wave limit, the base of the loop is fixed by the geometric coordinate $\rho_{\mathrm{L}} = h_2^2/h_1^2$, whereas the base of the corridor is determined by $\rho_{\mathrm{C}}(T)$, the density at which the singular condition $J \to \infty$ meets $k = 0$ (Sec. 2.3). Their ordering is controlled by the threshold $T_\times$, which exists only when $h_1 > h_2$. Loops are possible only while $\rho_{\mathrm{L}} < \rho_{\mathrm{C}}(T)$. Once $T > T_\times$, the ordering reverses and the loop collapses. For $h_2 > h_1$, one has $\rho_{\mathrm{C}}(T) \leq 1 < \rho_{\mathrm{L}}$ for all $T > 0$, so loop-type structures are excluded and only corridor-type formations remain.

A second organising parameter is the long-wave Bond threshold $T^* = h_1^2/3$, at which $\omega'' = 0$ and $J \to \infty$ coincide at $(\rho, k) = (0, 0)$. Below this value, gravity and capillarity act jointly, producing loop– and corridor–type structures with finite overlap. For $T > T^*$, the resonant ($J \to \infty$) and dispersive ($\omega'' = 0$) surfaces lie very close in a neighbourhood of the origin. When the depth ratio exceeds the golden value $h_2/h_1 = \varphi$, these surfaces develop a horizontal tangent at $(0, 0, T^*)$; for $h_2/h_1 > \varphi$, they acquire a local maximum in T. Planar sections then generate the capillary cut: a narrow corridor detached from the ρ–axis, characteristic of strongly capillary, upper–layer–dominated configurations.

The three-dimensional critical surfaces $J = 0$, $J \to \infty$ and $\omega'' = 0$ provide a single geometric framework for all observed structures. Loops, corridors, and cuts arise as planar intersections of these surfaces with planes $T = \text{const}$, and their evolution with varying T and depth ratio h_2/h_1 follows directly from the deformation of these surfaces. Two distinguished geometric configurations correspond to genuine degeneracies: equal layer depths ($h_1 = h_2$), where the resonant–dispersive intersection is a straight line, and the golden ratio ($h_2/h_1 = \varphi$), where the dispersive critical surface is horizontally tangent at $(0, 0, T^*)$. For $h_2/h_1 > \varphi$, this degeneracy evolves into a local maximum of the resonant–dispersive intersection curve and enables the onset of cut-type behaviour.

Overall, the results provide a coherent geometric framework for the classification of modulational stability in two-layer fluids with variable surface tension and extend the theory developed in Part I. They form a basis for future extensions involving shear, external forcing, flexible boundaries, or variable bathymetry.

Acknowledgments

Olga Avramenko thanks the Research Council of Lithuania for supporting this work.

ORCID

Olga Avramenko, https://orcid.org/0000-0002-7960-1436; **Volodymyr Naradovyi**, https://orcid.org/0000-0001-5187-8831

REFERENCES

[1] O. Avramenko and V. Naradovyi, East Eur. J. Phys. **3**, 239 (2025), https://doi.org/10.26565/2312-4334-2025-3-21.

[2] T. B. Benjamin, and J. E. Feir, J. Fluid Mech. **27**(3), 417 (1967). https://doi.org/10.1017/S002211206700045X

[3] V. E. Zakharov, J. Appl. Mech. Tech. Phys. **9**, 190 (1968). https://doi.org/10.1007/BF00913182

[4] R. H. J. Grimshaw, and D. I. Pullin, J. Fluid Mech. **160**, 297 (1985). https://doi.org/10.1017/S0022112085003494

[5] P. Christodoulides, and F. Dias, Phys. Fluids **7**, 3013 (1995). https://doi.org/10.1063/1.868678

[6] H. R. Dullin, G. A. Gottwald, and D. D. Holm, Fluid Dyn. Res. **33**, 73 (2003). https://doi.org/10.1016/S0169-5983(03)00046-7

[7] H. R. Dullin, G. A. Gottwald, and D. D. Holm, Physica D **190**, 1 (2004). https://doi.org/10.1016/j.physd.2003.11.004

[8] C. Sun, and E. Wahlén, arXiv:2509.17534 (2025). https://doi.org/10.48550/arXiv.2509.17534

[9] V. M. Hur, and J. Yang, arXiv:2311.01368 (2023). https://doi.org/10.48550/arXiv.2311.01368

[10] K. Ward, F. Zoueshtiagh, and R. Narayanan, Phys. Rev. Fluids **4**, 043903 (2019). https://doi.org/10.1103/PhysRevFluids.4.043903

[11] S. Li, A. Cao, J. Song, C. Yu, and J. Chen, Phys. Fluids **32**, 072104 (2020). https://doi.org/10.1063/5.0013225

[12] S. Li, X. Xie, D. Chen, and J. Song, Phys. Fluids **34**, 092105 (2022). https://doi.org/10.1063/5.0098077

[13] S. Murashige, and W. Choi, J. Fluid Mech. **938**, A13 (2022). https://doi.org/10.1017/jfm.2022.145

[14] T. Pal, and A. K. Dhar, Ocean Dyn. **72**, 241 (2022). https://doi.org/10.1007/s10236-022-01503-1

[15] T. Pal, and A. K. Dhar, Ocean Dyn. **74**, 133 (2024). https://doi.org/10.1007/s10236-023-01594-4

[16] S. Boral, B.-Y. Ni, and A.A. Korobkin, J. Fluid Mech. **1015**, A22 (2025). https://doi.org/10.1017/jfm.2025.10268

[17] S. Halder, M. Francius, A. K. Dhar, S. Mukherjee, H. C. Hsu, and C. Kharif, J. Fluid Mech. **1010**, A55 (2025). https://doi.org/10.1017/jfm.2025.318

[18] D. S. Goldobin, A. V. Pimenova, K. V. Kovalevskaya, D. V. Lyubimov, and T. P. Lyubimova, Phys. Rev. E **91**, 053010 (2015). https://doi.org/10.1103/PhysRevE.91.053010

[19] A. Doak, T. Gao, J.-M. Vanden-Broeck, and J. J. S. Kandola, Q. J. Mech. Appl. Math. **73**(3), 231 (2020). https://doi.org/10.1093/qjmam/hbaa009

[20] K. W. Chow, H. N. Chan, and R. H. J. Grimshaw, Nat. Hazards Earth Syst. Sci. **19**, 583 (2019). https://doi.org/10.5194/nhess-19-583-2019

[21] Y. Liang, A. Zareei, and M.-R. Alam, J. Fluid Mech. **811**, 400 (2017). https://doi.org/10.1017/jfm.2016.754

[22] S. Boral, T. Sahoo, and Y. Stepanyants, Symmetry **13**(4), 651 (2021). https://doi.org/10.3390/sym13040651

[23] O. L. Andreeva, L. A. Bulavin, and V. I. Tkachenko, East Eur. J. Phys. **2**, 38 (2020). https://doi.org/10.26565/2312-4334-2020-2-02.

[24] W. N. Bond, Philos. Mag. (Ser. 7) **4**(24), 889 (1927). https://doi.org/10.1080/14786441108564394

[25] F. Dias and C. Kharif, Annu. Rev. Fluid Mech. **31**, 301 (1999). https://doi.org/10.1146/annurev.fluid.31.1.301

[26] A. Davey and K. Stewartson, Proc. R. Soc. Lond. A **338**, 101 (1974). https://doi.org/10.1098/rspa.1974.0076

[27] O. Avramenko and V. Naradovyi, J. Appl. Math. Comput. Mech. **24**(2), 5 (2025), https://doi.org/10.17512/jamcm.2025.2.01.

[28] O. Avramenko and V. Naradovyi, Rend. Mat. Appl. (7) **47**, 55 (2026), https://doi.org/10.48550/arXiv.2411.15168.

НЕСТІЙКІСТЬ БЕНДЖАМІНА–ФЕЙРА МІЖФАЗНИХ ГРАВІТАЦІЙНО-КАПІЛЯРНИХ ХВИЛЬ У ДВОШАРОВІЙ РІДИНІ. ЧАСТИНА II. ВПЛИВ ПОВЕРХНЕВОГО НАТЯГУ

Ольга Авраменко[1,2], **Володимир Нарадовий**[3]
[1]*Національний університет "Києво-Могилянська академія вул. Сковороди, 2, Київ, 04070, Україна*
[2]*Університет Вітовта Великого, вул. К. Донелайчо, 58, Каунас, 44248, Литва*
[3]*Центральноукраїнський державний університет імені Володимира Винниченка,*
вул. Шевченка, 1, Кропивницький, 25006, Україна

У другій частині дослідження розроблено повний геометричний та асимптотичний опис того, як поверхневий натяг визначає модуляційну стійкість інтерфейсних хвиль у двошаровій рідині. Розвиваючи аналітичну схему Частини I, поверхневий натяг розглядається як вільний керівний параметр, що дає змогу відстежувати нелінійні та дисперсійні властивості системи для широкого діапазону співвідношень глибин та контрастів густин. Використовуючи зведення до нелінійного рівняння Шредінгера разом із довгохвильовими асимптотиками, визначено механізми, що формують межі між стабільними та нестабільними режимами, та встановлено їхню залежність від величини поверхневого натягу. Довгохвильова структура контролюється двома спеціальними значеннями густини, які задають точки зародження петлі та коридору на діаграмах стійкості. Взаємне розташування цих точок змінюється за певного порогу, що існує лише тоді, коли нижній шар є глибшим, і саме в цьому випадку можливе існування петлі. Другим організувальним параметром є класичний поріг Бонда, за якого дисперсійна і нелінійна сингулярності збігаються. Коли поверхневий натяг перевищує це значення і верхній шар є достатньо глибоким, взаємодія резонансних та дисперсійних ефектів утворює капілярний розріз, який заміщує коридор і характеризує режими з домінуванням капілярності. Для об'єднання цих спостережень побудовано повні тривимірні критичні поверхні, що розмежовують різні типи нелінійної та дисперсійної поведінки. Петля, коридор і розріз постають як площинні перерізи цих поверхонь, а їхні топологічні переходи безпосередньо зумовлені деформацією лінії перетину між резонансною та дисперсійною поверхнями. Два співвідношення глибин відповідають справжнім геометричним виродженням: рівні товщини шарів, коли лінія перетину стає прямою, та конфігурація золотого перетину, коли критична поверхня набуває горизонтальної дотичної при порозі Бонда. У цілому, Частина II завершує геометричну та фізичну класифікацію модуляційної стійкості інтерфейсних хвиль у двошарових рідинах і формує основу для подальших узагальнень, що враховують зсувні течії, зовнішні збурення, гнучкі межі або змінну батиметрію.

Ключові слова: *модуляційна нестійкість; міжфазні гравітаційно–капілярні хвилі; двошарова рідина; поверхневий натяг; нестійкість Бенджаміна–Фейра*